JOURNAL OF GEOPHYSICAL RESEARCH: ATMOSPHERES, VOL. 118, 1–15, doi:10.1002/jgrd.50803, 2013

A physically based analytical spatial air temperature and humidity model

Yang Yang,[1] Theodore A. Endreny,[1] and David J. Nowak[2]

Received 6 March 2013; revised 29 August 2013; accepted 30 August 2013.

[1] Spatial variation of urban surface air temperature and humidity influences human thermal comfort, the settling rate of atmospheric pollutants, and plant physiology and growth. Given the lack of observations, we developed a Physically based Analytical Spatial Air Temperature and Humidity (PASATH) model. The PASATH model calculates spatial solar radiation and heat storage based on semiempirical functions and generates spatially distributed estimates based on inputs of topography, land cover, and the weather data measured at a reference site. The model assumes that for all grids under the same mesoscale climate, grid air temperature and humidity are modified by local variation in absorbed solar radiation and the partitioning of sensible and latent heat. The model uses a reference grid site for time series meteorological data and the air temperature and humidity of any other grid can be obtained by solving the heat flux network equations. PASATH was coupled with the USDA iTree-Hydro water balance model to obtain evapotranspiration terms and run from 20 to 29 August 2010 at a 360 m by 360 m grid scale and hourly time step across a 285 km^2 watershed including the urban area of Syracuse, NY. PASATH predictions were tested at nine urban weather stations representing variability in urban topography and land cover. The PASATH model predictive efficiency R^2 ranged from 0.81 to 0.99 for air temperature and 0.77 to 0.97 for dew point temperature. PASATH is expected to have broad applications on environmental and ecological models.

Citation: Yang, Y., T. A. Endreny, and D. J. Nowak (2013), A physically based analytical spatial air temperature and humidity model, *J. Geophys. Res. Atmos.*, *118*, doi:10.1002/jgrd.50803.

1. Introduction

[2] Air temperature and humidity are important descriptors of terrestrial environmental condition [*Prihodko and Goward*, 1997] and they are two of the most critical meteorological variables in relation to biological and hydrological processes, human thermal comfort, ecosystems, and energy consumption on heating and cooling [*Shulman*, 1984; *Stahl et al.*, 2006]. Many studies show that land surface heterogeneity, such as local land cover and topography, has a significant effect on microscale air temperature and humidity [*Pielke*, 2001; *Weaver and Avissar*, 2001; *Lookingbill and Urban*, 2003; *Chun and Tamura*, 2005; *Solecki et al.*, 2005; *Robitu et al.*, 2006; *McCarthy et al.*, 2010; *Loridan and Grimmond*, 2012; *Yao and Steemers*, 2013]. The urban heat island, where urban area has higher temperature than surrounding rural areas [*Oke*, 1973; *Akbari et al.*, 1992; *Kim*, 1992; *Abramowitz et al.*, 2008; *Georgescu et al.*, 2012], exemplifies how land cover triggers spatial heterogeneity in air temperature; however, within-city variation of air temperature is ignored by most urban heat island conceptual models. Diurnal estimates of microclimate, particularly air temperature and humidity, are important for cities, which are home to 82.4% of the US population and upward of 77.7% of the population in many developing countries [*DESA*, 2012]. However, spatially detailed microscale maps (<500 m) of diurnal air temperature and humidity cannot be produced with standard diurnal weather station records because they are generally limited to single observations at meteorological stations.

[3] To obtain the microscale maps of air temperature and humidity, researchers have applied either observational measurement [*Takahashi et al.*, 2004; *Georgakis and Santamouris*, 2006] or numerical modeling [*Elnahas and Williamson*, 1997; *de La Flor and Domínguez*, 2004; *Bozonnet et al.*, 2005; *Robitu et al.*, 2006; *Yao et al.*, 2011]. The observational methods, including direct point measurement with high spatial density and indirect remote sensing measurement, place a significant demand on labor and instrumentation for measurements across large areas. Although remote sensing and infrared thermography can measure the spatially distributed surface skin temperature over large areas, studies show that there is no simple and general relationship between the patterns of surface skin temperature and air temperature [*Roth et al.*, 1989; *Stoll and Brazel*, 1992; *Eliasson*, 1996; *Jin et al.*, 2005]. *Voogt and Oke* [1997] concluded that regression techniques fail to predict air temperature based on remotely sensed skin surface temperature due

---

[1] Environmental Resources Engineering, SUNY ESF, Syracuse, New York, USA.

[2] USDA Forest Service Northern Research Station, Syracuse, New York, USA.

Corresponding author: Y. Yang, SUNY ESF, 321 Baker Labs, 1 Forestry Drive, Syracuse, NY 13210–2773, USA. (yyang31@syr.edu)

2169-897X/13/10.1002/jgrd.50803

to spatially variable and complex linkages between the two properties in urban areas. Moreover, due to the coarse temporal measurement interval of satellites, the temporal resolution of remote sensed maps would not satisfy hourly or daily time series needs of environmental applications. Numerical modeling has demonstrated great potential to map spatial air temperature and humidity fields. Computational Fluid Dynamics (CFD) simulations [*Dimoudi and Nikolopoulou*, 2003; *Mortensen et al.*, 2007; *Yao and Steemers*, 2013] or microclimate models, such as ENVI-met (http://www.envi-met.com/), use fluid dynamic equations to simulate heat and moisture fluxes, and can predict very detailed microclimate. However, due to the high computing time demand and intense data requirement for the CFD model domain, these models typically are applied to small spatial and temporal scale simulations. Regression models [*Chuanyan et al.*, 2005] and geostatistical models [*Ishida and Kawashima*, 1993; *Eliasson and Svensson*, 2003; *Lookingbill and Urban*, 2003] are also used to spatially distribute meteorological data, but these models are site specific and require extensive observed data for development.

[4] Land surface models overcome the limitations of observational and CFD or statistical numerical modeling methods in simulation of microscale spatially distributed air temperature and humidity. Land surface models were developed to better estimate the partitioning of energy into sensible heat flux and latent heat flux, but are generally applied in global or mesoscale climate models as the boundary layer representation. Land surface models are built on principles of energy balance and fluxes networks. The heat fluxes are determined by the temperature and humidity differences between vertical layers and are regulated by flux resistances. In the evolution of land surface models, representation of land surface morphology has incrementally improved from the bucket model [*Manabe*, 1969], big leaf model [*Monteith*, 1965; *Deardorff*, 1978], single layer model [e.g., *Dickinson et al.*, 1993; *Masson*, 2000; *Walko et al.*, 2000; *Chen and Dudhia*, 2001; *Kusaka et al.*, 2001], and multilayer model [e.g., *Ca et al.*, 1999; *Gu et al.*, 1999; *Wilson et al.*, 2003; *Krayenhoff et al.*, 2013]. The sophistication of land surface model flux balances has also evolved and includes hydrological, biophysical, biochemical, and ecological processes, such as the BATS (Biosphere-Atmosphere Transfer Scheme) [*Dickinson et al.*, 1993], SiB (Simple Biosphere Model) [*Sellers et al.*, 1986; *Sellers et al.*, 1996], NCAR LSM (The National Center for Atmospheric Research Land Surface Model) [*Bonan*, 1996], LEAF (Land Ecosystem-Atmosphere Feedback model) [*Lee*, 1992] and LEAF-2 [*Walko et al.*, 2000; *Fan et al.*, 2007; *Miguez-Macho et al.*, 2007; *Anyah et al.*, 2008], TEB (Town Energy Balance model) [*Masson*, 2000; *Hamdi and Masson*, 2008], and the ISAM (Integrated Science Assessment Model) [*Jain et al.*, 1996]. With the representation of various physical processes, land surface models not only improved the representation of the climate model boundary layer but were used in independent applications. For example, the LEAF-2 model was applied to estimate the global patterns of groundwater table depth [*Fan et al.*, 2013] and ISAM was used to study carbon storage and flux dynamics in the Amazon basin [*El-Masri et al.*, 2013]. Other land surface models use the canopy layer to explicitly represent the living environment of human beings [*Masson*, 2000; *Kusaka et al.*, 2001; *Lee and Park*, 2008] to simulate the temperature and humidity important to population centers. In the evolution of land surface models, they have arrived at a point where they can simulate the urban microclimate.

[5] The single layer Urban Canopy Model (UCM) coupled with Weather Research and Forecast (WRF) model has been applied to study the urban heat island in many major metropolitan regions [*Chen et al.*, 2011], such as Beijing, Hong Kong, Houston, New York City, Salt Lake City, Taipei, and Tokyo. *Chen et al.* [2011] found that formidable challenges limit application of this model, including initialization of the detailed spatial distribution of urban canopy state variables, such as temperature profiles within walls, roofs, and roads, and specification of a large number of parameters related to building characteristics, thermal properties, emissivity, and albedo. Moreover, land surface models such as UCM need spatially distributed meteorological forcing data that are not generally available for most urban areas, such as downward direct shortwave radiation, downward diffuse shortwave radiation, and downward longwave radiation. To satisfy these data needs, mesoscale climate models are generally used to provide time-series inputs for urban land surface models.

[6] Alternative methods to estimate spatial patterns of urban air temperature and humidity are needed to facilitate the growing interest in urban microclimatic response to land cover change. One method advanced by *Erell and Williamson* [2006] created the urban Canyon Air Temperature (CAT) model. The CAT model uses meteorological parameters monitored at one reference weather station to calculate the air temperature in another urban canyon by cross-comparing land cover. The CAT model assumes that the two sites are under the same mesoscale climatic conditions and the microclimate of the two sites is primarily modified by local land cover. Based on CAT model tests in Adelaide, Australia, it has achieved good simulations of the urban canyon air temperature in a range of weather conditions. However, the CAT model cannot simulate urban canyon humidity, a term important for human comfort and heat index calculations, and it requires detailed 3D description of the urban canyon to account for parameters such as the sky view factor, shading, and total urban surface area. The requirement for a 3D description of the urban canyon limited its application to small spatial scales.

[7] Our research builds on the CAT model and other urban land surface models (e.g., UCM and TEB) by combining their advantages of the single point weather measurement as input and a simplified urban canopy representation. In this research, we created the Physically based Analytical Spatial Air Temperature and Humidity (PASATH) model to simulate urban microclimate terms of air temperature and humidity at a subdaily time step. In section 2, we introduce the physics of the model; in section 3, we present an example application; in section 4, we discuss the advantages and limitations of the model; and in section 5, we summarize our research findings.

2. Model Development

2.1. Heat Flux Network

[8] The PASATH model calculates local grid air temperature and humidity by analytically solving the energy balance

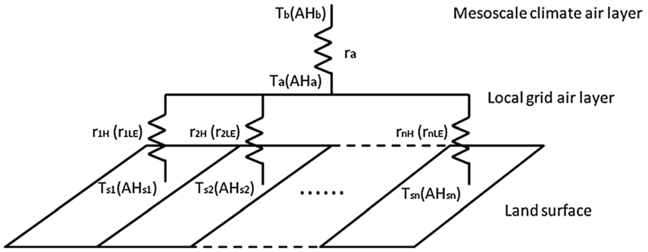

Figure 1. Energy flux net work above the land surface. The differences in temperature and humidity drive the energy fluxes between the land surface and local air, and between the local air and upper mesoscale air. T_{sn} and AH_{sn} represent the surface temperature and humidity of land cover n; T_a and AH_a represent the local air temperature and humidity; T_b and AH_b represent the mesoscale air temperature and humidity; r_a represents the heat transfer resistance between the local cluster air layer to the upper mesoscale air layer; and r_{nH} and r_{nLE} represent the sensible heat transfer resistance and latent heat transfer resistance between land surface and local air for land cover n.

equations describing the local vertical energy fluxes network (Figure 1). The vertical scale of this model is the surface layer, assumed to be a constant flux layer, which includes the canopy layer and the layer above the canopy. Our objective is to predict the air temperature and humidity in the canopy layer. The PASATH shares the following assumptions of the CAT model: (a) the aerodynamic mixing within the canopy is sufficient to allow the hypothetical existence of a mean canopy air stream, and the measured air temperature and humidity at the screen level (2 m) can represent the mean air temperature and humidity under the canopy; (b) there is a height above the canopy layer at which the temperature and humidity are approximately uniform. The PASATH model further assumes: a local grid can have n types of land cover, where common urban land cover types include impervious, soil, water, trees, and short vegetation; each land cover type is represented by simplified planar surface and is a percentage of the total grid area; the heat trapping effects of three-dimensional buildings and vegetation on absorption of solar radiation are represented by their effective albedos. In the development and illustration of the PASATH model, we use three land cover types (n), represented as subscripts 1, 2, 3, to demonstrate how the local grid air temperature and humidity are calculated. The energy flux network (Figure 1) can be described by the following equations:

$$H = \rho C_p \frac{T_a - T_b}{r_a} \tag{1}$$

$$LE = \lambda \frac{AH_a - AH_b}{r_a} \tag{2}$$

$$H_1 = \rho C_p \frac{T_{s1} - T_a}{r_{1H}} \tag{3}$$

$$LE_1 = \lambda \frac{AH_{s1} - AH_a}{r_{1LE}} \tag{4}$$

$$H_2 = \rho C_p \frac{T_{s2} - T_a}{r_{2H}} \tag{5}$$

$$LE_2 = \lambda \frac{AH_{s2} - AH_a}{r_{2LE}} \tag{6}$$

$$H_3 = \rho C_p \frac{T_{s3} - T_a}{r_{3H}} \tag{7}$$

$$LE_3 = \lambda \frac{AH_{s3} - AH_a}{r_{3LE}} \tag{8}$$

in which H (W/m^2) represents sensible heat flux and LE (W/m^2) represents latent heat flux between local grid air layer ($_a$) and mesoscale air layer ($_b$); H_n (W/m^2) represents sensible heat flux and LE_n (W/m^2) represents latent heat flux between land surface ($_s$) and local grid air layer ($_a$); ρ (kg/m^3) is the air density, C_p (J/kg/K) is the specific heat of air at constant pressure; λ (kJ/kg) is the latent heat of vaporization for water; T_{sn} and AH_{sn} represent the surface temperature and humidity, respectively, for land cover type n; T_a and AH_a represent the local air temperature and absolute humidity; T_b and AH_b represent the mesoscale air temperature and absolute humidity; r_a represents the heat transfer resistance between the canopy air layer to the upper mesoscale air layer; and r_{nH} and r_{nLE} represent the sensible heat transfer resistance and latent heat transfer resistance between land surface type n (1, 2, or 3 in this case) and canopy air.

[9] The energy budgets for each land cover type are:

$$Q_1^* + Q_{F1} = H_1 + LE_1 + \Delta Q_1 \tag{9}$$

$$Q_2^* + Q_{F2} = H_2 + LE_2 + \Delta Q_2 \tag{10}$$

$$Q_3^* + Q_{F3} = H_3 + LE_3 + \Delta Q_3 \tag{11}$$

in which Q_n^* (W/m^2) is the net all-wave radiation, Q_{Fn} (W/m^2) is anthropogenic heating, and ΔQ_n (W/m^2) is the heat storage for land cover type n. According to the conservation of energy and for steady state, the heat flux from local grid air layer to the mesoscale atmosphere should be equal to the summation of heat flux from each land cover to the local grid air layer:

$$H = C_1H_1 + C_2H_2 + C_3H_3 \tag{12}$$

$$LE = C_1LE_1 + C_2LE_2 + C_3LE_3 \tag{13}$$

in which C_n is the percentage for land cover type n. Assuming Q_n^*, Q_{Fn}, and ΔQ_n can be estimated based on physical and empirical values (introduced in section 2.2), and the heat flux resistances between the layers can be estimated based on semiempirical functions (introduced in section 2.3), then we have 13 equations and 18 unknown variables for n equal to three land cover types: H, LE, $H_{1\sim3}$, $LE_{1\sim3}$, T_a, AH_a, T_b, AH_b, $T_{s1\sim3}$, $e_{s1\sim3}$. To solve for the unknown variables, we need to either reduce the number of unknown variables or introduce additional equations to describe the system.

[10] The challenge remains to find the sensible heat flux, latent heat flux, surface temperature, and surface humidity variables. These variables are not commonly measured because of the difficulty of the measurements and the high operational and maintenance requirements of the instruments. To estimate these variables, we applied the underlying assumption of the Penman-Monteith potential evaporation equation that the surface temperature is approximately equal to the wet bulb temperature T_w and the surface humidity AH_{sn} is equal to the saturated humidity at wet bulb temperature $AH_{sat}(T_w)$. While the T_w term is cancelled during derivation of our model, this assumption allows us to derive a relationship between latent heat flux and sensible heat flux. According to the Penman-Monteith assumption, the potential latent heat flux PLE_n from land cover n can be described as:

$$PLE_n = \lambda \frac{AH_{sat}(T_w) - AH_a}{r_{nLE}} \tag{14}$$

[11] By introducing the slope of the saturation vapor pressure curve evaluated at air temperature T_a [*Maidment*, 1993]: $\Delta = \frac{AH_{sat}(T_a) - AH_{sat}(T_w)}{T_a - T_w}$, the saturated surface humidity can be described by:

$$AH_{sat}(T_w) \approx AH_{sat}(T_a) - \Delta(T_a - T_s) \tag{15}$$

[12] Inserting equation (15) into equation (14), we can obtain:

$$PLE_n = \lambda \frac{AH_{sat}(T_a) - \Delta(T_a - T_{sn}) - AH_a}{r_{nLE}} \tag{16}$$

[13] According to equations (3), (5), and (7), $T_a - T_{sn} = -\frac{H_n r_{nH}}{\rho C_p}$, and then the potential latent heat flux from land cover n (equation (16)) can be described by:

$$PLE_n = \lambda \frac{AH_{sat}(T_a) - AH_a}{r_{nLE}} + \lambda \frac{\Delta H r_{nH}}{r_{nLE}\rho C_p} \tag{17}$$

in which $AH_{sat}(T_a)$ is the air saturated absolute humidity (kg/m^3) at air temperature T_a (K) and can be calculated by [*Lawrence*, 2005]: $AH_{sat}(T_a) = \frac{1.324}{T_a} \times \exp\left(\frac{17.27(T_a - 273.15)}{(T_a - 35.85)}\right)$, Δ can be calculated by $\Delta = -\frac{AH_{sat}(T_a)\ (-4169.56 + \mathrm{T_a})\ (-0.308239 + \mathrm{T_a})}{T_a(-35.85 + T_a)^2}$, and AH_a is air absolute humidity calculated by:

$$AH_a = \frac{1.324}{T_d} \times \exp\left(\frac{17.27(T_d - 273.15)}{(T_d - 35.85)}\right) \tag{18}$$

in which T_d is dew point temperature. T_d is generally measured at standard weather station instead of air absolute humidity AH_a; therefore, we need equation (18) to covert T_d to AH_a. The potential latent heat flux calculated in equation (17) is then transformed into actual latent heat flux for each land cover type by representing constraints in water availability and resistances.

[14] The adjustment from potential to actual latent heat flux for impervious cover utilizes the water availability function developed by *Deardorff* [1978] and *Noilhan and Planton* [1989]. In place of the intercepted water on plant leaves, we consider the depression storage on impervious surfaces:

$$\begin{aligned} LE_{imp} &= PLE_{imp} * \left(\frac{S}{S_{\max}}\right)^{\frac{2}{3}} \\ &= \left(\lambda \frac{AH_{sat}(T_a) - AH_a}{r_{impLE}} + \lambda \frac{\Delta H r_{impH}}{r_{impLE}\rho C_p}\right) * \left(\frac{S}{S_{\max}}\right)^{\frac{2}{3}} \end{aligned} \tag{19}$$

in which S is the actual water storage depth of the impervious surface, S_{max} is the maximum depression storage depth of impervious surface, and r_{impLE} and r_{impH} are the aerodynamic resistance of latent heat and sensible heat flux above impervious surface. According to equation (19), the real latent heat flux from impervious surface is zero if there is no depression storage.

[15] The adjustment from potential to actual latent heat flux for bare soil cover uses root zone soil moisture storage and soil surface evaporation resistance as estimated by [*Beven et al.*, 1995; *Wang et al.*, 2008]:

$$\begin{aligned} LE_{soil} &= PLE_{Soil} * \frac{r_{SoilLE}}{r_{SoilLE} + r_g} * \left[1 - \left(\frac{D}{D_{\max}}\right)\right] \\ &= \left(\lambda \frac{AH_{sat}(T_a) - AH_a}{r_{SoilLE} + r_g} + \lambda \frac{\Delta \mathrm{H} r_{SoilH}}{(r_{SoilLE} + r_g)\rho C_p}\right) \\ &\quad * \left[1 - \left(\frac{D}{D_{\max}}\right)\right] \end{aligned} \tag{20}$$

in which D is the root zone water deficit depth, D_{max} is the maximum root zone water deficit depth, r_{soilLE} and r_{soilH} are the aerodynamic resistance of latent heat and sensible heat flux above soil surface, and r_g is soil surface evaporation resistance.

[16] The adjustment from potential to actual latent heat flux for vegetative cover is the summation of actual evaporation LE_{evap} and actual transpiration LE_{tran}:

$$LE_{Green} = LE_{evap} + LE_{tran} \tag{21}$$

[17] The actual evaporation LE_{evap} from intercepted precipitation can be estimated by [*Deardorff*, 1978; *Noilhan and Planton*, 1989]:

$$\begin{aligned} LE_{evapo} &= PLE_{Green} * \left(\frac{S}{S_{\max}}\right)^{\frac{2}{3}} \\ &= \left(\lambda \frac{AH_{sat}(T_a) - AH_a}{r_{GreenLE}} + \lambda \frac{\Delta H r_{GreenH}}{r_{GreenLE} \rho C_p}\right) * \left(\frac{S}{S_{\max}}\right)^{\frac{2}{3}} \end{aligned} \tag{22}$$

in which S is the intercepted precipitation depth per unit area, S_{max} is the maximum intercepted precipitation storage depth per unit area, and $r_{GreenLE}$ and r_{GreenH} are the aerodynamic resistance of latent heat and sensible heat flux above canopy. The actual transpiration LE_{tran} through the root, stem, and leaves is estimated by [*Liang et al.*, 1994]:

$$\begin{aligned} LE_{tran} &= PLE_{Green} * \frac{r_{GreenLE}}{r_{GreenLE} + r_c} * \left[1 - \left(\frac{S}{S_{\max}}\right)^{\frac{2}{3}}\right] \\ &= \left(\lambda \frac{AH_{sat}(T_a) - AH_a}{r_{GreenLE} + r_c} + \lambda \frac{\Delta H r_{GreenH}}{(r_{GreenLE} + r_c) \rho C_p}\right) \\ &\quad * \left[1 - \left(\frac{S}{S_{\max}}\right)^{\frac{2}{3}}\right] \end{aligned} \tag{23}$$

in which r_c is canopy resistance for transpiration.

[18] Using equations (19), (20), and (21) to express the relationship of latent heat flux and sensible heat flux in place of the six equations (3) to (8) gives us three fewer equations and six fewer variables (the surface temperature and surface humidity terms) to solve. Now we have 10 equations and 12 unknown variables. If we have a meteorological station located within the study area and local temperature T_a and humidity AH_a are measured, then for this local grid the number of unknown variables is reduced to 10. As a result, we have 10 equations (equations (1), (2), (9), (10), (11), (12), (13), (19), (20), and (21)) and 10 unknown variables, and we can solve these equations to obtain the values of H, LE, $H_{1\sim3}$, $LE_{1\sim3}$, T_b, AH_b. In our model development, we utilize the assumption of the Canopy Air Temperature (CAT) model [*Erell and Williamson*, 2006] that the mesoscale climate is homogenous for the study area. Therefore, for any other local grids, the calculated mesoscale air temperature T_b and humidity AH_b are known variables and the local air temperature T_a and humidity AH_a are unknown variables. By solving model equations (equations (1), (2), (9), (10), (11), (12), (13), (19), (20), and (21)), the local air temperature T_a and humidity AH_a can be obtained. The model simulation also provides the values for total latent heat flux LE, total sensible heat flux H, latent heat flux from every land cover $LE_{1\sim3}$, and sensible heat flux from every land cover $H_{1\sim3}$.

2.2. Estimation of Net All-Wave Radiation Q_n^*, Heat Storage ΔQ_n, and Anthropogenic Heating Q_{Fn}

2.2.1. Estimation of Net All-Wave Radiation Q_n^*

[19] The net all-wave radiation is composed of net shortwave radiation and net longwave radiation. It can be obtained by direct measurement, but it is not practical to measure it for every land grid for a spatially distributed model and it is not measured in most weather stations. In the PASATH model, we estimated the net all-wave radiation absorbed by each surface type Q_n^*, using the function [*Offerle et al.*, 2003]:

$$Q_n^* = L{\downarrow} - L{\uparrow} + SW(1 - \alpha) \tag{24}$$

in which $L\downarrow$ is the downward atmospheric longwave radiation, $L\uparrow$ is the upward longwave radiation, SW is the incoming shortwave radiation, and α is the land surface effective albedo. The incoming shortwave radiation for a particular land grid can be calculated by [*Kumar et al.*, 1997; *Kusaka et al.*, 2001]:

$$\begin{aligned} SW = SW_{Dir}[&\sin(\theta) * \cos(\varphi) * \sin(\delta) * \cos(\gamma) \\ &+ \sin(\theta) * \sin(\varphi) * \sin(\delta) * \sin(\gamma) \\ &+ \cos(\theta) * \cos(\delta)] + SW_{Dif} \end{aligned} \tag{25}$$

in which SW_{Dir} and SW_{Dif} are the direct solar radiation and diffuse solar radiation received by a horizontal surface; θ is the land slope; ϕ is land aspect; δ is the sun zenith angle; and γ is the sun azimuth angle. The hourly values of SW_{Dir} and SW_{Dif} are calculated using established algorithms [*Maxwell*, 1998] that consider the factors of sun position, cloud cover, aerosol optical length, precipitable water vapor, and ozone. The net direct shortwave radiation received by each land grid is calculated by including the influence of local *slope* and *aspect*, and the *zenith* and *azimuth* angle of the sun [*Kumar et al.*, 1997].

[20] The downward atmospheric longwave radiation is calculated according to the Stefan-Boltzmann law using air temperature T_a (K) [*Offerle et al.*, 2003]:

$$L{\downarrow} = \varepsilon_a \sigma T_a^4 \tag{26}$$

in which σ is the Stefan-Boltzman constant and ε_a is the atmosphere emissivity. The atmosphere emissivity ε_a is assumed related to air humidity and cloud cover percentage and estimated by $\varepsilon_a = [0.741 + (0.0062 * \mathrm{T_d})] * (1 - \mathrm{C}) + \mathrm{C}$, in which T_d is dew point temperature and C is the cloud cover percentage in the sky [*Berdahl and Fromberg*, 1982]. The upward longwave radiation is calculated by [*Offerle et al.*, 2003]:

$$L{\uparrow} = \varepsilon_s \sigma T_s^4 + (1 - \varepsilon_s) L{\downarrow} \tag{27}$$

in which ε_s is the surface emissivity. The PASATH model uses air temperature T_a (K) and incoming shortwave radiation to approximate the surface temperature [*Offerle et al.*, 2003]:

$$T_s^4 \approx T_a^4 + \frac{c * SW(1 - \alpha)}{\varepsilon_s \sigma} \tag{28}$$

in which c is a constant of 0.08 [*Offerle et al.*, 2003], SW is the incoming shortwave radiation, and α is the surface effective albedo. In equation (28), there is no adjustment of surface temperature during nighttime when *SW* is 0, and this is based on the study of *Offerle et al.* [2003] reporting a small nighttime difference of urban surface temperature and near surface air temperature.

2.2.2. The Estimation of Heat Storage ΔQ_n

[21] The heat storage ΔQ_n refers to the combined heat uptake and release from all substances, such as air, soil, biomass, and building materials. ΔQ_n for different land covers is estimated by using the empirical function [*Grimmond and Oke*, 1999a; *Grimmond and Oke*, 2002]:

$$\Delta Q_n = a_1 Q_n^* + a_2 \frac{\partial Q_n^*}{\partial t} + a_3 \tag{29}$$

in which t is the time, Q_n^* is the net all-wave radiation for land cover n, and a_1, a_2, and a_3 are empirical parameters. In the right-hand side of the equation, the first term represents the overall strength of the dependence of the heat storage on net radiation, the second term represents the phase difference of the heat storage and the net radiation, and the third term a_3 represents the spontaneous heat flux when both Q_n^* and $\frac{\partial Q_n^*}{\partial t}$ vanish, and may be caused by the temperature difference between land cover and air, or by the release of latent heat from land covers or air [*Camuffo and Bernardi*, 1982; *Erell and Williamson*, 2006]. The values of a_1, a_2, and a_3 relate to land use, surface materials and geometries, and the empirical values of a_1, a_2, and a_3 for different land cover types, including impervious, open, and green space, are provided by *Grimmond and Oke* [1999a].

2.2.3. The Estimation of Anthropogenic Heating Q_{Fn}

[22] The anthropogenic heating depends on various factors such as the intensity of energy use, power generation, and transportation systems [*Taha*, 1997]. *Sailor* [2011] identified methods to estimate anthropogenic heating as inventory approaches, energy budget closure methods, and building energy models. In a study of six large US cities, *Sailor and Lu* [2004] found that the maximum anthropogenic heating was 60 W/m^2 in the summer and 75 W/m^2 in winter. In our PASATH model, the anthropogenic heating can be specified by user-based knowledge of study site activities or can be safely neglected without introducing much error if its value is small or relative homogenous for the study area (see Appendix A for the mathematical evaluation). One tool to assist in these estimates is the LUCY (Large scale Urban Consumption of Energy) model [*Allen et al.*, 2011], which provides a rough estimate of the anthropogenic heating flux at spatial resolutions ranging from 30×30 arc-second to $0.5° \times 0.5°$, which includes several microclimate grids.

2.3. The Estimation of Heat Flux Resistances

[23] The wind speed under the urban canopy is assumed to have an exponential profile and the average wind speed is calculated by [*Kusaka et al.*, 2001]:

$$U_{can} = U_{top} \exp\left(-0.386 \frac{h}{w}\right) \tag{30}$$

in which U_{top} is the wind speed at the roof level, h is the building height, and w is the road width. The resistance for turbulent fluxes from the impervious or soil surface to urban canopy air layer is then estimated by [*Kusaka et al.*, 2001; *Lee and Park*, 2008]:

$$r_{\mathrm{Imp}H/LE} = r_{SoilH/LE} = \frac{\rho c_p}{11.8 + 4.2U_{can}} \tag{31}$$

[24] The resistance for turbulent fluxes between the vegetation layer and urban canopy layer is estimated by [*Lee and Park*, 2008]:

$$r_{GreenLE/H} = \frac{12(1 + 0.55LAI)U_{can}^{-1/2}}{1 - \exp(-0.4LAI)} \tag{32}$$

in which *LAI* is the vegetation Leaf Area Index.

[25] The wind profile above the urban canopy is assumed to have a logarithmic profile [*Kusaka et al.*, 2001], and the aerodynamic resistances of latent heat and sensible heat fluxes above the urban canopy are treated the same [*Lindroth*, 1993]:

$$r_a = \frac{\ln^2\left(\frac{z_u - d}{z_o}\right)}{k^2 u_z} \tag{33}$$

in which z_u is the wind speed measurement height, d is the zero plane displacement of the logarithmic wind profile, z_o is a roughness length governing the transfer of heat and water, k is the von-Karman constant 0.4, and u_z is the wind speed measured at the z_u height. The aerodynamic properties of the urban area have been studied intensely [*Grimmond*, 1998; *Grimmond and Oke*, 1999b; *Millward-Hopkins et al.*, 2011; *Crago et al.*, 2012]; however, there is no generic formula for the roughness length and zero plane displacement for heterogeneous urban settings. Some experimental studies suggests the roughness length range 0.4 to 0.7 m for dense low buildings and 0.7 to 1.5 m for regularly built towns [*Wiernga*, 1993; *Masson*, 2000], with a value approximating one tenth of the building height. In the PASATH model, we set the default roughness length to one tenth of average building height, but users can specify the values of roughness length and zero plane displacement based on their knowledge of their study area.

[26] The surface resistance for soil evaporation r_g is calculated as [*Sellers et al.*, 1992]:

$$r_g = \exp\left(8.206 - 4.255 \frac{\theta - \theta_{wp}}{\theta_{sat} - \theta_{wp}}\right) \tag{34}$$

in which θ is soil volumetric water content, θ_{wp} is the soil wilting point, and θ_{sat} is the saturated water content. According to equation (34), as the soil dries, the resistance for soil evaporation increases. The canopy resistance r_c is estimated by [*Liang et al.*, 1994]:

$$r_c = \frac{r_{c,\min} * g}{LAI} \tag{35}$$

in which *LAI* is leaf area index, $r_{c,min}$ is the minimum canopy resistance, and $g^{-1} = \frac{\theta - \theta_{wp}}{\theta_{fc} - \theta_{wp}}$ where θ_{fc} is soil field capacity and θ_{wp} is soil wilting point. The value of θ can range from wilting point for completely dry condition to the value of θ_{sat} for saturated condition.

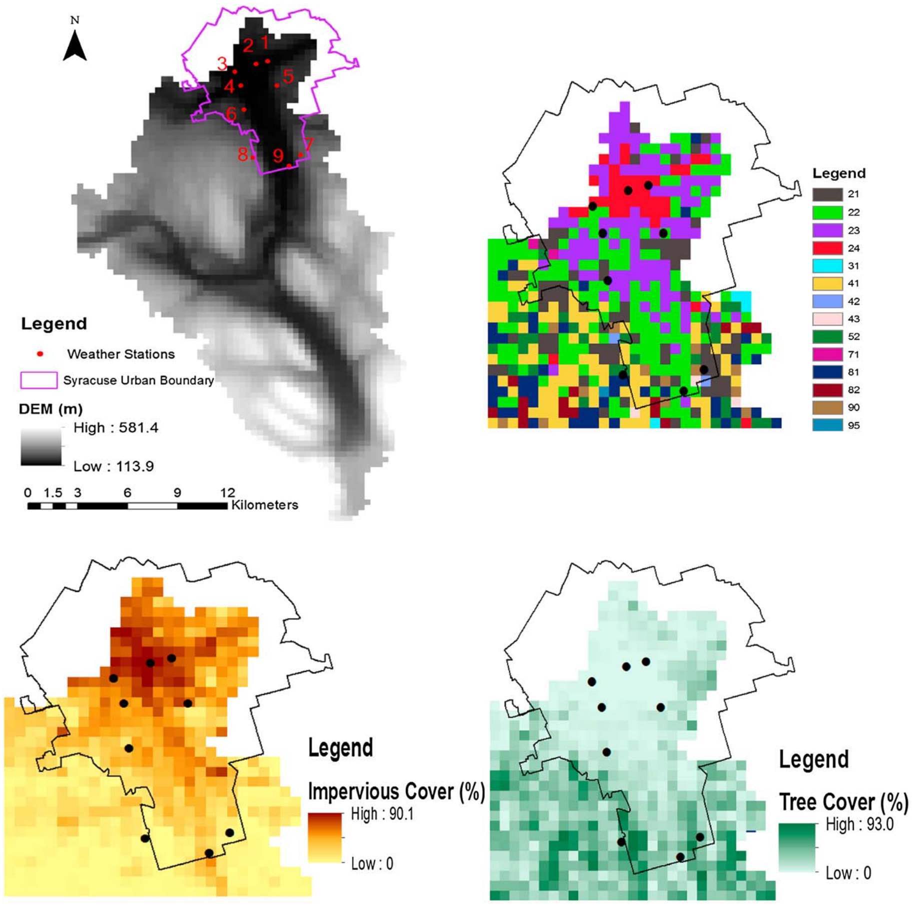

Figure 2. Top left figure is Onondaga Creek watershed study site with elevation data and weather stations, top right is the Syracuse, NY city area with 2001 National Land Cover Data (codes 21–24 are developed, codes 41–43 are forested). Bottom left is the city area with percent impervious cover and bottom right is city area with percent canopy cover. All cover data are shown at 360 m resolution pixels.

3. PASATH Model Application

3.1. Study Site

[27] The PASATH model was designed to use hydrological information of water availability for each land grid at each time step. We provided this information by coupling PASATH with the watershed scale hydrology model iTree-Hydro [*Wang et al.*, 2005; *Wang et al.*, 2008; *Yang et al.*, 2011]. The iTree-Hydro model uses TOPMODEL spatial water redistribution concepts [*Beven and Kirkby*, 1979] to simulate the lateral flow of ground water along with urban and vegetation interception functions to represent the impact of land cover on soil moisture. iTree-Hydro has flexible spatial resolution, limited by land cover and elevation maps (e.g., 1 to 100 m). The PASATH and iTree-Hydro models were coupled through the evapotranspiration terms; at each time step, iTree-Hydro simulates the water storage of each grid and then PASATH simulates the evapotranspiration and updates the water storage of each grid. We applied the coupled model to the 285 km^2 Onondaga Creek watershed (outlet at USGS Spencer Street gauge. #04240010, 43°2′49″N 76°8′40″W), with 53% forest cover, 32% agricultural cover, 14% urban cover, and 1% water cover, and which contains much of the city of Syracuse, NY. Syracuse, NY is 50 km south of the eastern edge of Lake Ontario and has a humid continental climate. US Census data estimate the 2010 population of Syracuse at 147,306, which is the fifth most populous city in the state of New York. Interest in Syracuse air temperature and humidity motivated the USDA Forest Service to deploy nine local weather stations throughout the Syracuse urban area in 2010, placing the stations to sample the variability in topography and land cover (Figure 2 and Table 1). The weather stations are in inner-city low-lying plains with varying building and tree canopy cover, a residential site in a flat valley, and upland areas of residential, institutional, forest, and park land cover. The measured under canopy air temperature and humidity were taken at 2 m height. Our tests of PASATH model accuracy assume that the station measured air temperature and humidity represent the average value of the simulated grid. The PASATH model input of topography was obtained from digital elevation model (DEM) data, and the input of land cover (Figure 2) was obtained using the 2001 National Land Cover Database (NLCD), noting the fraction of tree canopy and impervious surface in each NLCD land cover grid. We resampled the original 30 m resolution NLCD maps to 360 m by 360 m resolution (12 × 12 NLCD pixels) to incorporate a larger influence area for each simulated land grid. For grids not classified as water (NLCD codes 11 and 12), if the combined fraction of impervious cover and tree

Table 1. National Land Cover Data Type, Impervious Cover Fraction, and Tree Canopy Cover Fraction at the Weather Station Sites

Site		NLCD Land Use	Impervious Cover (%)	Tree Canopy Cover (%)
1	Reference	24: Developed, High Intensity	79.9	0.0
2	CBD	24: Developed, High Intensity	89.7	0.0
3	West side, N	22: Developed, Low Intensity	62.0	0.0
4	West side, S	23: Developed, Medium Intensity	52.0	3.3
5	Campus	22: Developed, Low Intensity	64.7	1.9
6	Park	22: Developed, Low Intensity	31.6	14.3
7	Suburban	52: Shrub/Scrub	4.8	42.9
8	Forest	21: Developed, Open Space	2.9	45.2
9	Valley	22: Developed, Low Intensity	26.1	21.8

canopy cover was less than 1, we assigned the remaining fraction to short vegetation for all land cover classes except barren cover (NLCD code 31) which is assigned to bare soil. The inputs values for PASATH model parameters are shown in Table 2. There are four categories for urban area used in our 2001 NLCD land cover classification: developed, open space (NLCD code 21), developed, low intensity (NLCD code 22), developed, medium intensity (NLCD code 23), and developed, high intensity (NLCD code 24). For each of the four urban categories, we assigned different values for building height to road width ratio (h/w). The city of Syracuse is a medium-sized city with low buildings and broad roads. The residential area is featured with sparse two-story houses and the urban core has higher buildings of which the heights typically do not exceed six stories. We do not have detailed in situ measurement of building heights and road widths, but even with such measurements it is difficult to parameterize the values for a large area. In this study, the values of h/w were assigned around the values used by TEB model for a medium-sized city [*Masson*, 2000]. These values can be calibrated if necessary. The impervious cover effective albedo was assigned using relations between effective albedo and h/w [*Masson*, 2000]. The USDA FS weather station 1 was located in developed high intensity land cover (NLCD code 24) and was arbitrarily chosen as the reference site to calculate the mesoscale climate. The PASATH model simulated air temperature and humidity across the entire watershed, and predicted and observed values were compared at the eight weather stations at an hourly time step.

3.2. Simulation Results

[28] The air temperature, humidity, sensible heat flux, and latent heat flux of each local grid were simulated by PASATH model. We evaluated the simulation results from two aspects: (a) whether the PASATH model accurately simulated spatial variations in air temperature and humidity; (b) whether the PASATH model accurately simulated the local grid air temperature and humidity.

[29] Changes in elevation and land cover across the watershed created between-station variation in both observed air temperature and dew point temperature, which ranged by about 6 K (Figure 3); the between-station variation is the difference between the local weather station value and the reference weather station value. The smallest variation in temperature was during 23 August when winds were highest and rains were present (Figure 3). To evaluate the capability of the PASATH model to capture spatial variations in air temperature and dew point temperature, we contrast between-station variations of both simulated air temperature and simulated dew point temperature (Figure 3). Compared

Table 2. The PASATH Model and Coupled iTree-Hydro Model Parameter Values

Symbol	Name (Unit)	Value
Θ_{wp}	Soil wilting point (%)	0.05
Θ_{fc}	Soil field capacity (%)	0.2
Θ_{sat}	Soil saturation point (%)	0.35
$r_{c,min}$	Canopy minimum resistance (s/m)	150
z_u	Wind measurement height (m)	10
α_{tree}	Effective albedo of tree	0.15
α_{short}	Effective albedo of short vegetation	0.25
α_{soil}	Effective albedo of soil	0.17
ε_{veg}	Emissivity of vegetation (tree or short vegetation)	0.97
ε_{soil}	Emissivity of soil	0.95
ε_{imp}	Emissivity of impervious	0.95
α_{imp21}	Effective albedo of impervious for developed open space area	0.4
α_{imp22}	Effective albedo of impervious for developed low intensity area	0.25
α_{imp23}	Effective albedo of impervious for developed medium intensity area	0.18
α_{imp24}	Effective albedo of impervious for developed high intensity area	0.15
h_{imp21}	Average urban canopy height for developed open space (m)	0.1
h_{imp22}	Average urban canopy height for developed low intensity area (m)	5
h_{imp23}	Average urban canopy height for developed medium intensity area(m)	10
h_{imp24}	Average urban canopy height for developed high intensity area (m)	15
$(h/w)_{imp21}$	Average building height to road width ratio for developed open space area	0.01
$(h/w)_{imp22}$	Average building height to road width ratio for developed low intensity area	0.5
$(h/w)_{imp23}$	Average building height to road width ratio for developed medium intensity area	0.8
$(h/w)_{imp24}$	Average building height to road width ratio for developed high intensity area	1.2

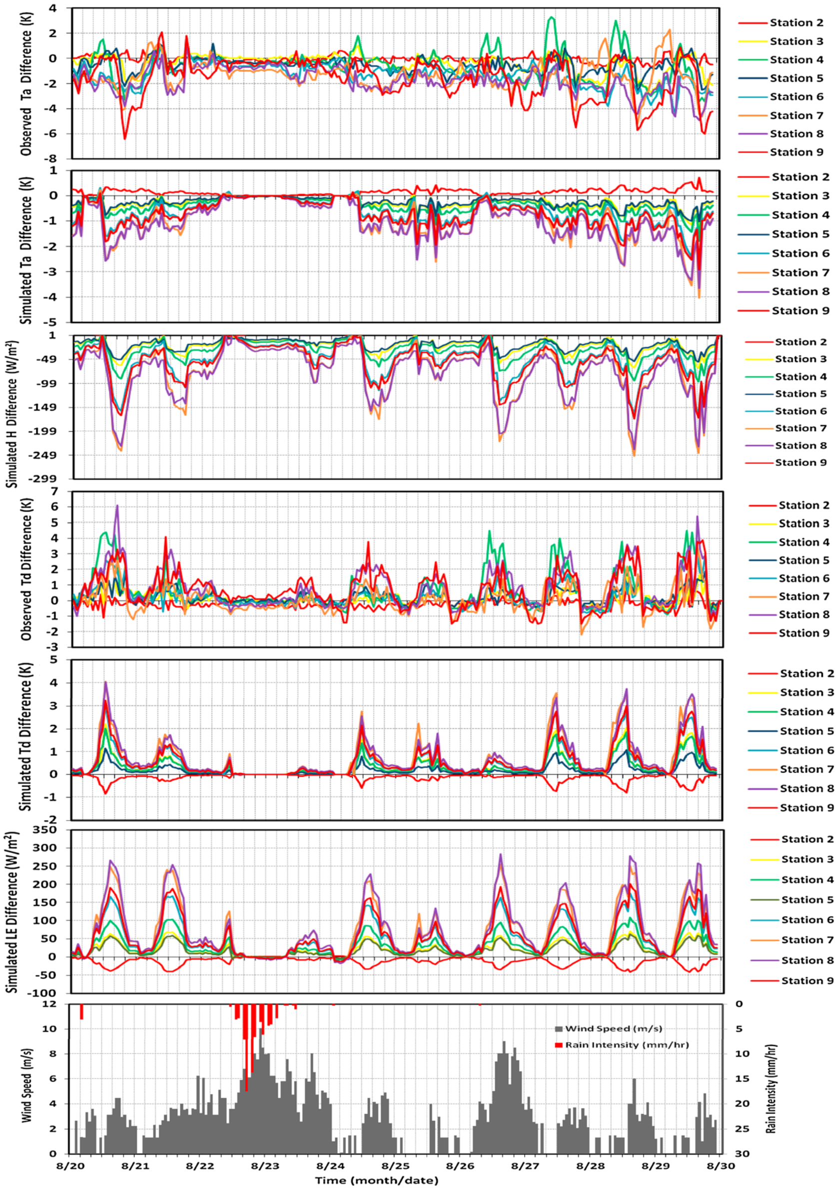

Figure 3. Between-station variation (station n - station 1) of observed air temperature, simulated air temperature, simulated sensible heat, observed dew point temperature, simulated dew point temperature, and simulated latent heat, and observed wind speed and rain for time period 20 to 29 August 2010 for all the stations.

with 6 K between-station variation in the observed air temperature, the simulated air temperature only varied by 4 K. This difference is explained by simulation controls, which according to equation (1) include sensible heat flux from the local air layer to the mesoscale air layer and the aerodynamic resistance. Between-station variation can be examined by applying equation (1) to any two grids 1 and 2, such that:

$$H_1 = \rho C_p \frac{T_{a1} - T_b}{r_a} \tag{36}$$

$$H_2 = \rho C_p \frac{T_{a2} - T_b}{r_a} \tag{37}$$

in which T_{a1} and T_{a2} are the local air temperature for land grids 1 and 2. By subtracting equation (37) from equation (36), we get:

$$H_1 - H_2 = \rho C_p \frac{T_{a1} - T_{a2}}{r_a} \tag{38}$$

[30] The sensible heat flux difference ($H_1 - H_2$) between grids 1 and 2 can be represented by the local air temperature difference, ($T_{a1} - T_{a2}$). The simulated sensible heat flux has between-station variation ranging by 250 W/m^2 (Figure 3). Using the relation equation (38) for an aerodynamic resistance of 25 s/m, we computed that a 250 W/m^2 difference in sensible heat flux leads to a 6 K difference in simulated air temperature. According to equation (33) the aerodynamic resistance is determined by the wind speed when the urban morphology is fixed; the higher the wind speed, the lower the aerodynamic resistance. Given the wind measurement height of 10 m, zero displacement height is 6 m and roughness length is 1 m; with the wind speed of 1 m/s, the

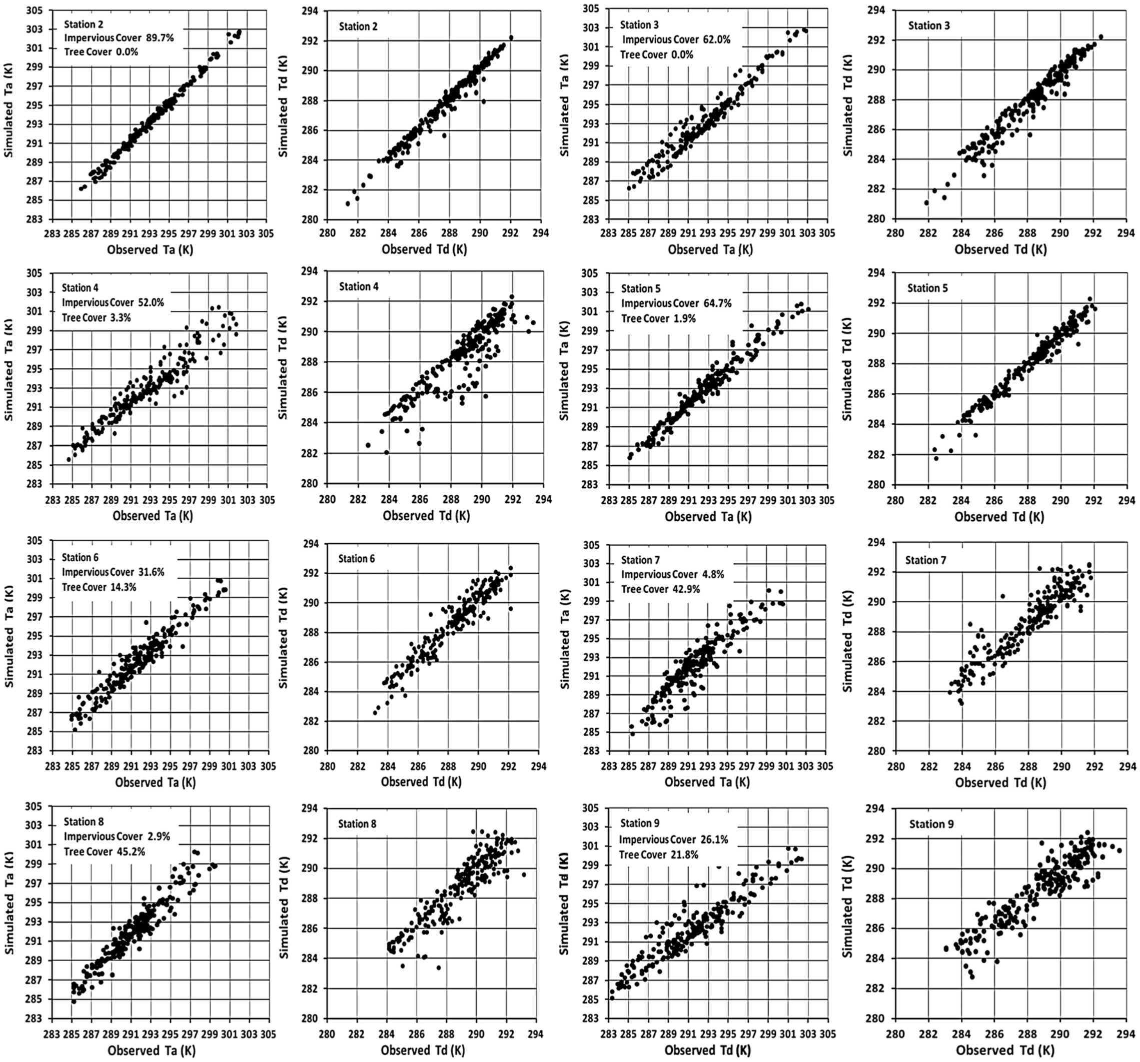

Figure 4. Scatterplots of simulated air temperature and humidity for station 2 to station 9.

aerodynamic resistance is 12 s/m and a 250 W/m^2 difference in sensible heat flux leads to a 3 K difference in simulated air temperature. When the wind speed is 5 m/s, the aerodynamic resistance is lowered to 2.4 s/m and a 250 W/m^2 difference in sensible heat flux leads to a 0.6 K difference in simulated air temperature. For example, we had large simulated between-station variations of sensible heat flux (about 220 W/m^2) at 16:00 26 August that are explained by high wind speeds creating a low aerodynamic resistance and led to only 1 K between-station variation of simulated air temperature, while the observed variation was nearly 4 K and station winds varied.

[31] Between-station variation in simulated dew point temperature ranged by 4 K (Figure 3), and between-station variations of observed and simulated dew point temperature were larger in daytime than nighttime. This is explained by simulated daytime variations in latent heat flux ranging by 300 W/m^2, while nighttime maximum variation was only 50 W/m^2. Between-station variation of dew point

Table 3. Correlation Coefficient (R^2) of Simulated Air Temperature and Dew Point Temperature Time Series and R^2 of Reference Site Observed Air Temperature and Dew Point Temperature Time Series

Site		Simulated Air Temperature R^2	Reference Site Air Temperature R^2	Simulated Dew Point Temperature R^2	Reference Site Dew Point Temperature R^2
2	CBD	0.99	0.99	0.97	0.97
3	West side, N	0.96	0.94	0.97	0.95
4	West side, S	0.9	0.86	0.78	0.6
5	Campus	0.96	0.94	0.97	0.94
6	Park	0.89	0.77	0.9	0.86
7	Suburban	0.82	0.64	0.77	0.84
8	Forest	0.85	0.54	0.83	0.52
9	Valley	0.81	0.7	0.84	0.67

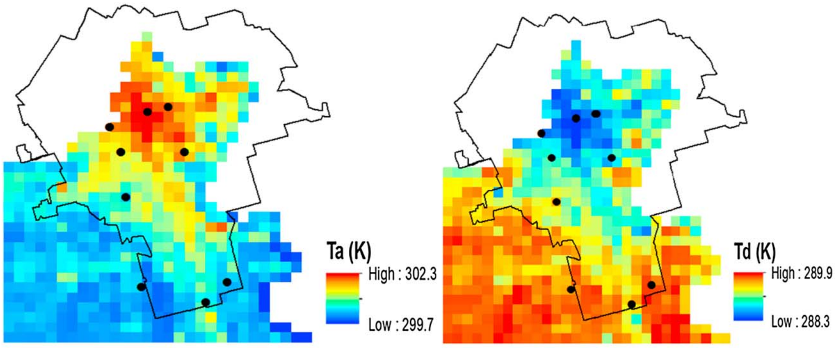

Figure 5. Simulated spatial air temperature (Ta) and dew point temperature (Td) at 17:00 29 August 2010.

temperature can be examined by applying equation (2) and equation (18) in an analysis similar to that for sensible heat flux (equations (36) and (37)). In this case we find the between-station variations in simulated latent heat flux are reflected by variation in simulated dew point temperature. During nighttime, the net all-wave radiation was generally low and provided little energy for latent heat flux, so the absolute between-station differences of latent heat flux were small. As a result, both observed and simulated dew point temperature exhibited smaller nighttime between-station variation than daytime variation.

[32] During rain events, from 22 August at 12:00 pm to 23 August at 1:00 pm (Figure 3), both the simulated air temperature and dew point temperature had very small between-station variation, and matched the observed variation. This agreement was attributed to the synoptic nature of the precipitation with nearly uniform radiation and high wind speed across the entire watershed.

[33] To show and evaluate the accuracy of simulated local grid air temperature and humidity, we plotted the scatterplots of the simulated air temperature and dew point temperature for each weather station (Figure 4). Because dew point temperature was recorded instead of the absolute humidity at the nine weather stations, equation (18) was used to covert simulated absolute humidity to dew point temperature. From direct observations of the plots (Figure 4), we can see that the simulation can capture the observed air temperature and dew point temperature for each station, with better fit for stations with higher impervious cover. We used the R^2 metric to quantify fit between simulated and observed values, where a value of 1 represents perfect correspondence and a value of 0 indicates that the observed average is a better estimator than the simulation. The R^2 values ranged from 0.81 to 0.99 for simulated air temperature and from 0.77 to 0.97 for simulated dew point temperature (Table 3). The R^2 values were higher for stations with higher impervious cover percentage (e.g., station 2, station 3, and station 5) than for stations with higher tree cover percentage (e.g., station 7 and station 8). This decrease in model performance with increasing vegetation cover may be caused by errors associated with vegetation related parameters, such as canopy resistance and *LAI*.

[34] We also tested whether simulated temperatures were a better estimator of observed values than using the reference site weather as an estimator by calculating the R^2 values for the observed air temperature and dew point temperature at the reference site and all observed weather station locations (Table 3). According to the R^2 values, we can conclude that the simulated air temperature was always a better estimator of local air temperature than the reference site observed air temperature. The PASATH model simulated dew point temperature was a better estimator of local dew point temperature than the reference site observed dew point temperature for all the stations except for station 7 (NLCD 52: Shrub/Scrub), which may be caused by errors on shrub-related parameters, such as shrub *LAI* or shrub canopy resistance. The overall simulation accuracy at each weather station site is determined on the estimation accuracy of the inputs of the PASATH model, such as the effective albedo of impervious and vegetation cover, land cover percentages, water availability on each land cover, incident solar energy, wind speed, *h*/*w*, and heat storage. Better estimation of the input variables can improve the model prediction on the local grid air temperature and humidity.

[35] Spatial distributions of the PASATH model simulated air temperature and dew point temperature can be generated at any time step, and we present the spatial maps for 17:00 on 29 August 2010 in Figure 5. The simulated maximum spatial difference in air temperature was about 2.6 K, and the spatial difference in dew point temperature was about 1.6 K. Air temperature spatial distributions had a negative correlation with tree canopy cover and positive correlation with impervious cover, while dew point temperature had an opposite trend. This spatial pattern matches the typical inverse trend between air and dew point temperature due to the differences in water availability and the partitioning of net radiation into sensible and latent heat. These spatial phenomena illustrate how vegetation can maintain lower air temperatures and provide more moisture to the air.

4. Discussion

[36] Our PASATH model used a flat surface representation of land cover rather than the 3D geometry of buildings and trees, and this simplification provides great computational efficiency with little cost to predictive accuracy. A study of 12 sites in Chicago, Los Angeles; Mexico City, Miami, Sacramento, Tucson, and Vancouver by *Grimmond and Oke* [1999a] found that incorporating 3D effects into their Objective Hysteresis Model (OHM) did not significantly improve model predictive accuracy for energy flux and storage prediction. Moreover, although the 3D descriptions for some large cities in the US will be available through the National Urban database and Access Portal Tool (NUDAPT) in the near future [*Ching et al.*, 2009], generally

the 3D descriptions of buildings and trees have large data requirements, and even with LiDAR data they are difficult to generate for a city or watershed scale application. The tradeoff of using 3D surfaces also increases the complexity of the model and introduces more parameters to estimate, which may cause other, perhaps larger, errors to simulation results. The flat surface scheme applied in this PASATH model allows model application in any region with 2D land cover maps.

[37] Area of influence in the PASATH model simulations was a critical component in the model scheme, regulating how much influence local slope and aspect as well as impervious and vegetation cover had on grid weather patterns. *Mizuno et al.* [1991] found that the influence radius for local climate ranged from 50 to 200 m for their five Japanese case studies, carried out in summer, autumn and winter of 1990. In our simulations in August 2010 for Syracuse NY we examined areas of influence of 30 by 30 m, 90 by 90 m, 180 by 180 m, and 360 by 360 m, where larger grids incorporate a larger area of influence on the local climate. In these PASATH simulations, we found that the model accuracy for air temperature and dew point temperature was not consistent across time and space. Our between-simulation variation in spatial predictive accuracy was sensitive to grid resolution because spatial variation in geometry regulated the area of influence; local elevation maxima may have smaller areas of influence than broad valleys or building intense area may have smaller areas of influence than open area. The temporal variation in the predictive accuracy was due to the impact of weather conditions on the area of influence; e.g., windy conditions often extend the area of influence. It is impossible to identify an optimal spatial resolution for all locations and all simulation periods, but we found that microclimate was smoothed with overly coarse resolution grids, and the influence of neighboring areas is lost with overly fine resolution grids. For our geography, climate, and period of study, we recommend a grid resolution between 200 and 400 m to generate an appropriate area of influence.

[38] Land cover differences in the PASATH model, such as impervious cover and vegetation cover, are characterized by effective albedo, heat storage, and evaporation terms. Smaller effective albedo results in greater trapping of solar radiation. Vegetation generally has a lower albedo than impervious cover; however, the effective albedo of 3D buildings increases nonlinearly with an increase in the ratio of building height to road width (h/w). *Masson* [2000] investigated the relationship of urban canyon effect albedo and canyon shape by the TEB model and found that when the albedo of road and wall is 0.4, the effective albedo of urban canyon can decrease to 0.02 when h/w increased to 3. Parameterization of the heat storage term followed the study of *Grimmond and Oke* [2002], which found that impervious cover had larger heat storage than vegetation cover, given the same amount of net solar radiation. We did not explicitly consider anthropogenic heating in our application as it is included implicitly in the reference site air temperature input, and we demonstrate mathematically (see Appendix A) that neglecting anthropogenic heating Q_F introduces very small error to the estimated air temperature when the anthropogenic heating is small or relative homogenous for the study area (our case). When the anthropogenic heating values have large spatial differences (~10^3 W/m^2) within the simulation domain, then neglecting anthropogenic heating can cause large errors (1–2°C) in simulated temperature, as found in Tokyo [*Sailor and Lu*, 2004].

[39] Evaporation on impervious cover only occurred when water was available in surface depression storage. For vegetation, the evapotranspiration only occurred when soil water content was above the soil moisture wilting point. Therefore, given the same amount of net radiation, more energy is converted to sensible heat flux on impervious areas than on vegetated areas, and dry impervious Bowen Ratios resemble desert condition values. Therefore, for areas receiving the same amount net radiation, the area with greater vegetation cover will have lower air temperature and higher humidity or dew point temperature. Similar conclusions were reached by other numerical studies [*Honjo and Takakura*, 1991; *Shashua-Bar and Hoffman*, 2000].

[40] We derived the relationship of the wet surface latent heat flux and the sensible heat flux (equation (17)) based on the assumption in the Penman-Monteith potential evaporation equation that the surface temperature is approximated by the wet bulb temperature [*Maidment*, 1993]. *Vercauteren et al.* [2009] obtained a similar relationship between wet surface latent heat flux and sensible heat flux by linearization of the Bowen Ratio. We further related the actual latent heat flux to potential latent heat flux by empirical functions for different land covers. The explicit expression of the relationship of latent heat flux and sensible heat flux (equation (17)) can be used to estimate the latent heat flux where the function variables, such as the water storage, air temperature, humidity, wind speed, heat flux resistance, and the sensible heat flux, can be measured or estimated [*Vercauteren et al.*, 2009].

[41] The local temperature simulation accuracy of PASATH model is determined by the simulation accuracy of heat flux terms and the aerodynamic resistance terms influenced by winds. In this study, we applied coarse estimation of the land cover percentages, heat storage, building height to road width ratio, and effective albedo, which can cause errors on the estimation of the heat flux terms. Our PASATH model simulation and testing revealed the importance of local wind on observed and estimated air temperature and humidity. Wind speed is a critical parameter in aerodynamic resistance of heat fluxes. We will incorporate atmosphere stability corrections on aerodynamic resistance calculation in the future version of PASATH.

5. Conclusions

[42] We developed a 2D Physically based Analytical Spatial Air Temperature and Humidity (PASATH) model based on the heat flux network above the land surface. The PASATH model assumes that the mesoscale climate is homogenous and quantifies the influence of topography, impervious cover, and vegetation cover on local air temperature. The PASATH model was coupled with a spatially distributed watershed hydrology model, iTree-Hydro, to constrain local grid water storage and evaporation terms. The coupled PASATH and iTree-Hydro model was tested in the urban area of Syracuse, NY watershed from 20 to 29 August 2010 at a 360 m grid resolution and 1 h time step. Simulation results were compared with nine weather stations measuring the microclimate at distinct land cover and elevation areas. The PASATH model performed satisfactorily given its intended simplicity. The PASATH model has low data requirements to meet typical

urban data constraints: elevation data, land cover data, rough average building height and *h*/*w* estimates, and basic time-series weather data (air temperature, humidity, and wind speed) measured in a reference site. The model can be used to study urban heat island effects and investigate land cover and hydrology-based mitigation methods. The PASATH model can spatially map air temperature and humidity for other environmental models, including atmospheric models, ecosystem models, and hydrology models, for scientific studies of environmental and human health.

Appendix A: Mathematical Evaluation of the Impacts of Anthropogenic Heating Q_F on the Prediction of the Urban Canopy Air Temperature

[43] If we consider the anthropogenic heating Q_F explicitly, the sensible heat flux from urban canopy of the reference site to mesoscale air layer can be described by:

$$H_0 + \Delta H_0 = \rho C_p \frac{T_{a0} - T_{b00}}{r_0} \tag{A1}$$

in which H_0 is the sensible heat flux from solar energy, ΔH_0 is the sensible heat flux contributed by anthropogenic heating, T_{a0} is the measured air temperature in the reference site, T_{b00} is the predicted mesoscale air temperature if the anthropogenic heating is considered explicitly, and r_0 is the aerodynamic resistance. Then T_{b00} can be calculated by:

$$T_{b00} = T_{a0} - r_0 \frac{H_0 + \Delta H_0}{\rho C_p} \tag{A2}$$

[44] For another site, the sensible heat flux is also described by equation A1 with the same mesoscale air temperature T_{b00} and site-specific values for other variables. Therefore, the air temperature can be calculated by the transformation of equation A1 and use equation A2 to take place of T_{b00}:

$$\begin{aligned} T_{a10} &= r_1 \frac{H_1 + \Delta H_1}{\rho C_p} + T_{b00} \\ &= T_{a0} - r_0 \frac{H_0}{\rho C_p} - r_0 \frac{\Delta H_0}{\rho C_p} + r_1 \frac{H_1}{\rho C_p} + r_1 \frac{\Delta H_1}{\rho C_p} \end{aligned} \tag{A3}$$

in which ΔH_1 is the sensible heat flux contributed by anthropogenic heating and r_1 is the aerodynamic resistance. If we do not consider the anthropogenic heating explicitly, the sensible heat flux from the urban canopy of the reference site to mesoscale air layer can be described by:

$$H_0 = \rho C_p \frac{T_{a0} - T_{b01}}{r_0} \tag{A4}$$

[45] Transformation of equation A4 generates the predicted mesoscale air temperature when the anthropogenic heating is not considered explicitly:

$$T_{b01} = T_{a0} - r_0 \frac{H_0}{\rho C_p} \tag{A5}$$

[46] The predicted air temperature for another site T_{a11} can be described by:

$$T_{a11} = r_1 \frac{H_1}{\rho C_p} + T_{b01} = T_{a0} - r_0 \frac{H_0}{\rho C_p} + r_1 \frac{H_1}{\rho C_p} \tag{A6}$$

[47] By comparing equation A3 and equation A6, we see that the predicted air temperature when the anthropogenic heating is considered (equation A3) has two more terms $-r_0 \frac{\Delta H_0}{\rho C_p}$ and $r_1 \frac{\Delta H_1}{\rho C_p}$ than the predicted air temperature when the anthropogenic heating is not explicitly considered (equation A6). If the ΔH_0, ΔH_1, and aerodynamic resistance are the same for the two sites, the two terms cancel and the predicted air temperatures have the same value. When the difference of the anthropogenic heating is 50 W/m^2, the difference of ΔH_0 and ΔH_1 will be much less because of the partitioning of the anthropogenic heating to heat storage and latent heat flux. For example, if the final value of the difference of ΔH_0 and ΔH_1 is 20 W/m^2 and the aerodynamic resistance is 10 s/m, then the prediction error will be just 0.1–0.2 K. Therefore, the ignorance of anthropogenic heating in our application would only introduce very small error on the air temperature simulation.

[48] **Acknowledgments.** This research was supported by funding from the USDA Forest Service Northern Research Station iTree Spatial Simulation grant PL-5937 and the National Urban and Community Forest Advisory Council iTree Tool grant 11-DG-11132544-340. The SUNY ESF Department of Environmental Resources Engineering provided computing facilities and logistical support.

References

Abramowitz, G., R. Leuning, M. Clark, and A. Pitman (2008), Evaluating the performance of land surface models, *J. Clim.*, *21*(21), 5468–5481, doi:10.1175/2008jcli2378.1.

Akbari, H., S. Davis, J. Huang, P. Liu, and H. Taha (1992), The urban heat island: Causes and impacts, in *Cooling Our Communities, A Guidebook on Tree Planting and Light-Colored Surfacing*, edited by H. Akbari et al., pp. 5–26, U.S. Environmental Protection Agency, Washington, D.C.

Allen, L., F. Lindberg, and C. Grimmond (2011), Global to city scale urban anthropogenic heat flux: Model and variability, *Int. J. Climatol.*, *31*(13), 1990–2005.

Anyah, R. O., C. P. Weaver, G. Miguez-Macho, Y. Fan, and A. Robock (2008), Incorporating water table dynamics in climate modeling: 3. Simulated groundwater influence on coupled land-atmosphere variability, *J. Geophys. Res.*, *113*, D07103, doi:10.1029/2007JD009087.

Berdahl, P., and R. Fromberg (1982), The thermal radiance of clear skies, *Sol. Energy*, *29*(4), 299–314.

Beven, K., and J. Kirkby (1979), A physically based, variable contributing area model of basin hydrology, *Hydrol. Sci. Bull.*, *24*(1), 43–69.

Beven, K., R. Lamb, P. Quinn, R. Romanowics, and J. Freer (1995), TOPMODEL, in *Computer Models of Watershed Hydrology*, edited by V. P. Singh, pp. 627–688, Water Resources Publications, Colo.

Bonan, G. B. (1996), Land surface model (LSM version 1.0) for ecological, hydrological, and atmospheric studies: Technical description and users guide., *Technical Rep.*, National Center for Atmospheric Research, Boulder, CO (United States). Climate and Global Dynamics Div., Boulder, CO, USA.

Bozonnet, E., R. Belarbi, and F. Allard (2005), Modelling solar effects on the heat and mass transfer in a street canyon, a simplified approach, *Sol. Energy*, *79*(1), 10–24.

Ca, V. T., T. Asaeda, and Y. Ashie (1999), Development of a numerical model for the evaluation of the urban thermal environment, *J. Wind Eng. Ind. Aerodyn.*, *81*(1), 181–196.

Camuffo, D., and A. Bernardi (1982), An observational study of heat fluxes and their relationships with net radiation, *Boundary Layer Meteorol.*, *23*(3), 359–368.

Chen, F., and J. Dudhia (2001), Coupling an advanced land-surface/hydrology model with the Penn State/NCAR MM5 modeling system. Part I: Model implementation and sensitivity, *Mon. Weather Rev.*, *129*, 569–585.

Chen, F., H. Kusaka, R. Bornstein, J. Ching, C. Grimmond, S. Grossman-Clarke, T. Loridan, K. W. Manning, A. Martilli, and S. Miao (2011), The integrated WRF/urban modelling system: Development, evaluation, and applications to urban environmental problems, *Int. J. Climatol.*, *31*(2), 273–288.

Ching, J., M. Brown, T. McPherson, S. Burian, F. Chen, R. Cionco, A. Hanna, T. Hultgren, D. Sailor, and H. Taha (2009), National urban database and access portal tool, *Bull. Am. Meteorol. Soc.*, *90*(8), 1157–1168.

Chuanyan, Z., N. Zhongren, and C. Guodong (2005), Methods for modelling of temporal and spatial distribution of air temperature at landscape scale in the southern Qilian mountains, China, *Ecol Model*, *189*(1), 209–220.

Chun, C., and A. Tamura (2005), Thermal comfort in urban transitional spaces, *Build. Environ.*, *40*(5), 633–639.

Crago, R. D., W. Okello, and M. F. Jasinski (2012), Equations for the drag force and aerodynamic roughness length of urban areas with random building heights, *Boundary Layer Meteorol.*, *145*(3), 423–437.

Deardorff, J. W. (1978), Efficient prediction of ground surface temperature and moisture with inclusion of a layer of vegetation, *J. Geophys. Res.*, *83*, 889–1903.

DESA (2012), World urbanization prospects: The 2011 revision, in *Population*, edited by U. Nations, United Nations Publications, N.Y.

de La Flor, F. S., and S. A. Domínguez (2004), Modelling microclimate in urban environments and assessing its influence on the performance of surrounding buildings, *Energy Build.*, *36*(5), 403–413.

Dickinson, R. E., P. Kennedy, and A. Henderson-Sellers (1993), Biosphere-atmosphere transfer scheme (BATS) version 1e as coupled to the NCAR community climate model, *Technical Rep. NCAR/TN-387+STR*, National Center for Atmospheric Research, Climate and Global Dynamics Division, Boulder, CO, USA, doi:10.5065/D67W6959.

Dimoudi, A., and M. Nikolopoulou (2003), Vegetation in the urban environment: microclimatic analysis and benefits, *Energy Build.*, *35*(1), 69–76.

Eliasson, I. (1996), Urban nocturnal temperatures, street geometry and land use, *Atmos. Environ.*, *30*(3), 379–392.

Eliasson, I., and M. Svensson (2003), Spatial air temperature variations and urban land use-a statistical approach, *Meteorol. Appl.*, *10*(02), 135–149.

El-Masri, B., R. Barman, P. Meiyappan, Y. Song, M. Liang, and A. K. Jain (2013), Carbon dynamics in the Amazonian Basin: Integration of eddy covariance and ecophysiological data with a land surface model, *Agric. For. Meteorol.*, doi:10.1016/j.agrformet.2013.1003.1011.

Elnahas, M., and T. J. Williamson (1997), An improvement of the CTTC model for predicting urban air temperatures, *Energy Build.*, *25*(1), 41–49.

Erell, E., and T. Williamson (2006), Simulating air temperature in an urban street canyon in all weather conditions using measured data at a reference meteorological station, *Int. J. Climatol.*, *26*(12), 1671–1694.

Fan, Y., G. Miguez-Macho, C. P. Weaver, R. Walko, and A. Robock (2007), Incorporating water table dynamics in climate modeling: 1. Water table observations and equilibrium water table simulations, *J. Geophys. Res.*, *112*, D10125, doi:10.1029/2006JD008111.

Fan, Y., H. Li, and G. Miguez-Macho (2013), Global patterns of groundwater table depth, *Science*, *339*(6122), 940–943.

Georgakis, C., and M. Santamouris (2006), Experimental investigation of air flow and temperature distribution in deep urban canyons for natural ventilation purposes, *Energy Build.*, *38*(4), 367–376.

Georgescu, M., M. Moustaoui, A. Mahalov, and J. Dudhia (2012), Summertime climate impacts of projected megapolitan expansion in Arizona, *Nat. Clim. Change*, *3*(1), 37–41.

Grimmond, C. (1998), Aerodynamic roughness of urban areas derived from wind observations, *Boundary Layer Meteorol.*, *89*(1), 1–24.

Grimmond, C., and T. R. Oke (1999a), Heat storage in urban areas: Local-scale observations and evaluation of a simple model, *J. Appl. Meteorol.*, *38*(7), 922–940.

Grimmond, C. S. B., and T. R. Oke (1999b), Aerodynamic properties of urban areas derived from analysis of surface form, *J. Appl. Meteorol.*, *38*(9), 1262–1292.

Grimmond, C., and T. R. Oke (2002), Turbulent heat fluxes in urban areas: Observations and a local-scale urban meteorological parameterization scheme (LUMPS), *J. Appl. Meteorol.*, *41*(7), 792–810.

Gu, L., H. H. Shugart, J. D. Fuentes, T. Black, and S. R. Shewchuk (1999), Micrometeorology, biophysical exchanges and NEE decomposition in a two-story boreal forest—Development and test of an integrated model, *Agric. For. Meteorol.*, *94*(2), 123–148.

Hamdi, R., and V. Masson (2008), Inclusion of a drag approach in the Town Energy Balance (TEB) scheme: Offline 1D evaluation in a street canyon, *J. Appl. Meteorol. Climatol.*, *47*(10), 2627–2644.

Honjo, T., and T. Takakura (1991), Simulation of thermal effects of urban green areas on their surrounding areas, *Energy Build.*, *15*(3), 443–446.

Ishida, T., and S. Kawashima (1993), Use of cokriging to estimate surface air temperature from elevation, *Theor. Appl. Climatol.*, *47*(3), 147–157.

Jain, A. K., H. S. Kheshgi, and D. J. Wuebbles (1996), A globally aggregated reconstruction of cycles of carbon and its isotopes, *Tellus B*, *48*(4), 583–600.

Jin, M., R. E. Dickinson, and D. Zhang (2005), The footprint of urban areas on global climate as characterized by MODIS, *J. Clim.*, *18*(10), 1551–1565.

Kim, H. H. (1992), Urban heat island, *Int. J. Remote Sens.*, *13*(12), 2319–2336.

Krayenhoff, S., A. Christen, A. Martilli, and T. Oke (2013), A multi-layer radiation model for urban neighbourhoods with trees, *Urban Clim. News*, *47*, 7–11.

Kumar, L., K. S. Andrew, and E. Knowles (1997), Modelling topographic variation in solar radiation in a GIS environment, *Int. J. Geogr. Inf. Sci.*, *11*(5), 475–497.

Kusaka, H., H. Kondo, Y. Kikegawa, and F. Kimura (2001), A simple single-layer urban canopy model for atmospheric models: Comparison with multi-layer and slab models, *Boundary Layer Meteorol.*, *101*(3), 329–358.

Lawrence, M. G. (2005), The relationship between relative humidity and the dewpoint temperature in moist air: A simple conversion and applications, *Bull. Am. Meteorol. Soc.*, *86*, 225–233.

Lee, T. J. (1992), The impact of vegetation on the atmospheric boundary layer and convective storms, PhD thesis, 155 pp, Colorado State University, CO, USA.

Lee, S.-H., and S.-U. Park (2008), A vegetated urban canopy model for meteorological and environmental modelling, *Boundary Layer Meteorol.*, *126*(1), 73–102.

Liang, X., D. P. Lettenmaier, E. Wood, and S. Burges (1994), A simple hydrologically based model of land surface water and energy fluxes for general circu-lation models, *J. Geophys. Res.*, *99*, 14,415–14,428.

Lindroth, A. (1993), Aerodynamic and canopy resistance of short-rotation forest in relation to leaf area index and climate, *Boundary Layer Meteorol.*, *66*(3), 265–279.

Lookingbill, T. R., and D. L. Urban (2003), Spatial estimation of air temperature differences for landscape-scale studies in montane environments, *Agric. For. Meteorol.*, *114*(3), 141–151.

Loridan, T., and C. Grimmond (2012), Multi-site evaluation of an urban land-surface model: Intra-urban heterogeneity, seasonality and parameter complexity requirements, *Q. J. R. Meteorol. Soc.*, *138*(665), 1094–1113.

Maidment, D. R. (1993), *Handbook of Hydrology*, McGraw-Hill, New York.

Manabe, S. (1969), Climate and the ocean circulation: 1. The atmospheric circulation and the hydrology of the Earth's surface, *Mon. Weather Rev.*, *97*(11), 739–774.

Masson, V. (2000), A physically-based scheme for the urban energy budget in atmospheric models, *Boundary Layer Meteorol.*, *94*(3), 357–397.

Maxwell, E. (1998), METSTAT—The solar radiation model used in the production of the National Solar Radiation Data Base (NSRDB), *Sol. Energy*, *62*(4), 263–279.

McCarthy, M. P., M. J. Best, and R. A. Betts (2010), Climate change in cities due to global warming and urban effects, *Geophys Res Lett*, *37*, L09705, doi:10.1029/2010GL042845.

Miguez-Macho, G., Y. Fan, C. P. Weaver, R. Walko, and A. Robock (2007), Incorporating water table dynamics in climate modeling: 2. Formulation, validation, and soil moisture simulation, *J. Geophys. Res.*, *112*, D13108, doi:10.1029/2006JD008112.

Millward-Hopkins, J., A. Tomlin, L. Ma, D. Ingham, and M. Pourkashanian (2011), Estimating aerodynamic parameters of urban-like surfaces with heterogeneous building heights, *Boundary Layer Meteorol.*, *141*(3), 443–465.

Mizuno, M., Y. Nakamura, H. Murakami, and S. Yamamoto (1991), Effects of land use on urban horizontal atmospheric temperature distributions, *Energy Build.*, *15*(1–2), 165–176.

Monteith, J. L. (1965), Evaporation and environment, *Symp. Soc. Exp. Biol.*, *19*, 245–269.

Mortensen, L. H., M. Woloszyn, C. Rode, and R. Peuhkuri (2007), Investigation of microclimate by CFD modeling of moisture interactions between air and constructions, *J. Build. Phys.*, *30*(4), 279–315.

Noilhan, J., and S. Planton (1989), A simple parameterization of land surface processes for meteorological models, *Mon. Weather Rev.*, *117*, 536–549.

Offerle, B., C. Grimmond, and T. R. Oke (2003), Parameterization of net all-wave radiation for urban areas, *J. Appl. Meteorol.*, *42*(8), 1157–1173.

Oke, T. R. (1973), City size and the urban heat island, *Atmos. Environ.*, *7*, 769–779.

Pielke, R. A. (2001), Influence of the spatial distribution of vegetation and soils on the prediction of cumulus convective rainfall, *Rev. Geophys.*, *39*(2), 151–177.

Prihodko, L., and S. N. Goward (1997), Estimation of air temperature from remotely sensed surface observations, *Remote Sens. Environ.*, *60*(3), 335–346.

Robitu, M., M. Musy, C. Inard, and D. Groleau (2006), Modeling the influence of vegetation and water pond on urban microclimate, *Sol. Energy*, *80*(4), 435–447.

Roth, M., T. Oke, and W. Emery (1989), Satellite-derived urban heat islands from three coastal cities and the utilization of such data in urban climatology, *Int. J. Remote Sens.*, *10*(11), 1699–1720.

Sailor, D. J. (2011), A review of methods for estimating anthropogenic heat and moisture emissions in the urban environment, *Int. J. Climatol.*, *31*(2), 189–199.

Sailor, D. J., and L. Lu (2004), A top–down methodology for developing diurnal and seasonal anthropogenic heating profiles for urban areas, *Atmos. Environ.*, *38*(17), 2737–2748.

Sellers, P., Y. Mintz, Y. C. Sud, and A. Dalcher (1986), A simple biosphere model (SiB) for use within general circulation models, *J. Atmos. Sci.*, *43*(6), 505–531.

Sellers, P., J. Berry, G. Collatz, C. Field, and F. Hall (1992), Canopy reflectance, photosynthesis, and transpiration. III. A reanalysis using improved leaf models and a new canopy integration scheme, *Remote Sens. Environ.*, *42*(3), 187–216.

Sellers, P., D. Randall, G. Collatz, J. Berry, C. Field, D. Dazlich, C. Zhang, G. Collelo, and L. Bounoua (1996), A revised land surface parameterization (SiB2) for atmospheric GCMs. Part I: Model formulation, *J. Clim.*, *9*(4), 676–705.

Shashua-Bar, L., and M. E. Hoffman (2000), Vegetation as a climatic component in the design of an urban street—An empirical model for predicting the cooling effect of urban green areas with trees, *Energy Build.*, *31*(3), 221–235.

Shulman, M. D. (1984), Microclimate—The biological environment, *Soil Sci.*, *138*(3), 256.

Solecki, W. D., C. Rosenzweig, L. Parshall, G. Pope, M. Clark, J. Cox, and M. Wiencke (2005), Mitigation of the heat island effect in urban New Jersey, *Global Environ. Change Part B: Environ. Hazards*, *6*(1), 39–49.

Stahl, K., R. Moore, J. Floyer, M. Asplin, and I. McKendry (2006), Comparison of approaches for spatial interpolation of daily air temperature in a large region with complex topography and highly variable station density, *Agric. For. Meteorol.*, *139*(3), 224–236.

Stoll, M., and A. Brazel (1992), Surface-air temperature relationships in the urban environment of Phoenix, Arizona, *Phys. Geogr.*, *13*(2), 160–179.

Taha, H. (1997), Urban climates and heat islands: Albedo, evapotranspiration, and anthropogenic heat, *Energy Build.*, *25*(2), 99–103.

Takahashi, K., H. Yoshida, Y. Tanaka, N. Aotake, and F. Wang (2004), Measurement of thermal environment in Kyoto city and its prediction by CFD simulation, *Energy Build.*, *36*(8), 771–779.

Vercauteren, N., E. Bou-Zeid, H. Huwald, M. B. Parlange, and W. Brutsaert (2009), Estimation of wet surface evaporation from sensible heat flux measurements, *Water Resour Res*, *45*, W06424, doi:10.1029/2008WR007544.

Voogt, J. A., and T. R. Oke (1997), Complete urban surface temperatures, *J. Appl. Meteorol.*, *36*(9), 1117–1132.

Walko, R. L., L. E. Band, J. Baron, T. G. Kittel, R. Lammers, T. J. Lee, D. Ojima, R. A. Pielke Sr., C. Taylor, and C. Tague (2000), Coupled atmosphere-biophysics-hydrology models for environmental modeling, *J. Appl. Meteorol.*, *39*(6), 931–944.

Wang, J., T. A. Endreny, and J. M. Hassett (2005), Flexible modeling package for topographically based watershed hydrology, *J. Hydrol.*, *314*(1–4), 78–91.

Wang, J., T. A. Endreny, and D. J. Nowak (2008), Mechanistic simulation of tree effects in an urban water balance model, *J. Am. Water Resour. Assoc.*, *44*(1), 75–85.

Weaver, C. P., and R. Avissar (2001), Atmospheric disturbances caused by human modification of the landscape, *Bull. Am. Meteorol. Soc.*, *82*(2), 269–281.

Wiernga, J. (1993), Representative roughness parameters for homogeneous terrain, *Boundary Layer Meteorol.*, *63*(4), 323–363.

Wilson, T., J. Norman, W. Bland, and C. Kucharik (2003), Evaluation of the importance of Lagrangian canopy turbulence formulations in a soil–plant–atmosphere model, *Agric. For. Meteorol.*, *115*(1), 51–69.

Yang, Y., T. A. Endreny, and D. J. Nowak (2011), iTree-Hydro: Snow hydrology update for the urban forest hydrology model, *J. Am. Water Resour. Assoc.*, *47*(6), 1,211–1,218.

Yao, R., and K. Steemers (2013), Urban microclimates and simulation, in *Design and Management of Sustainable Built Environments*, edited by R. Yao, pp. 77–97, Springer, London.

Yao, R., Q. Luo, and B. Li (2011), A simplified mathematical model for urban microclimate simulation, *Build. Environ.*, *46*(1), 253–265.